ResearchGate

See discussions, stats, and author profiles for this publication at: https://www.researchgate.net/publication/356315814

On the numerical study of fatigue process in rail heads by means of an isotropic damage based high-cycle fatigue constitutive law

Article *in* Engineering Failure Analysis · November 2021

DOI: 10.1016/j.engfailanal.2021.105915

CITATIONS
0

READS
69

4 authors:

Sergio Jiménez
Universitat Politècnica de Catalunya
5 PUBLICATIONS **10** CITATIONS
SEE PROFILE

Lucia Gratiela Barbu
Universitat Politècnica de Catalunya
16 PUBLICATIONS **98** CITATIONS
SEE PROFILE

Sergio Oller
Universitat Politècnica de Catalunya
268 PUBLICATIONS **6,801** CITATIONS
SEE PROFILE

Alejandro Cornejo
Universitat Politècnica de Catalunya
14 PUBLICATIONS **49** CITATIONS
SEE PROFILE

Some of the authors of this publication are also working on these related projects:

Base Isolation and Energy Dissipation View project

Pasarela peatonal sobre el río Besós. View project

All content following this page was uploaded by Alejandro Cornejo on 20 November 2021.

The user has requested enhancement of the downloaded file.

On the numerical study of fatigue process in rail heads by means of an isotropic damage based high-cycle fatigue constitutive law

S. Jiménez[a,b,*], L. G. Barbu[a,b], S. Oller[a,c], A. Cornejo[a,b]

[a] *Centre Internacional de Mètodes Numèrics en Enginyeria (CIMNE), Campus Norte UPC, 08034 Barcelona, Spain*
[b] *Universidad Politécnica de Cataluña (UPC), Campus Norte UPC, 08034 Barcelona, Spain*
[c] *Consejo Nacional y de Investigaciones Científicas y Técnicas (CONICET), Facultad de Ingeniería, Universidad Nacional de Salta, Av. Bolivia 5150, 4400, Salta, Argentina*

Abstract

The fatigue phenomenon has been historically related to the railway industry. Nowadays, thanks to the high quality of the materials used, most of the recorded problems have been overcome although there are still degradation processes which are associated to fatigue and need to be considered for the definition of the maintenance campaigns and the general progress of the sector. In this paper, the latest improvements in the isotropic damage based high-cycle fatigue constitutive law proposed by Oller et al. [1] are presented and the approach is used for the study of two regions of the railway path where fatigue mechanisms are experimentally detected: a straight section and a crossing element. The analysis of the affected areas is performed through a finite element simulation identifying the critical regions liable to the fatigue degradation when the structure interacts with high speed vehicles and predicting the initiation of the degradation at the rail head while capturing the physics of the problem. The potential of the methodology is shown through the case studies and the current shortcomings and the future lines of research are clearly stated.

Keywords: railway, finite element method, high-cycle fatigue simulation, isotropic damage, advance in time strategy, pearlitic steel, Hadfield steel

*Corresponding author.
Email address: sjimenez@cimne.upc.edu (S. Jiménez)

1. Introduction

Since the second half of the $19th$ century, the fatigue phenomenon has been deeply studied, originally associating it to the recurrent deterioration detected in the railway system which led to unexpected failures [2]. In this process the mechanical properties of the material are progressively degraded when cyclic loads below the ultimate material strength are applied [3, 4].

Nowadays, fatigue is determining in the failure of elements and structures in aerospace, naval and car industries as well as in some structures within the civil engineering field [4, 5]. The variety and complexity of the scenarios where these failures take place [6, 7, 8, 9, 10, 11, 12, 13, 14] make it necessary to develop numerical tools that allow for the correct study and prediction of the phenomenon. In this paper, a constitutive law based on the continuum damage mechanics and dedicated to the study of High-Cycle Fatigue (HCF) processes is presented and used for the study of one of these failure scenarios. HCF is a specific typology of fatigue characterized by the large number of cycles that lead to failure ($10^5 - 10^7$ cycles) and by the conditions at which it takes place. This fatigue process occurs without the presence of plastic deformations and failure takes place in a brittle manner, driven by the coalescence of internal pores [1, 15]. Therefore, the problem has been historically approached from the damage mechanics point of view in several ways [4, 16, 17].

The main objective of the undergone research has been to confront the presented HCF model towards real railway structures where fatigue degradation is detected, in particular it is devoted to study the degradation observed at the wheel-rail interaction region.

The paper is organized in several sections, starting by introducing in Sections 2 and 3 the problem that motivates the undergone research and the methodology applied, respectively. The degradation process, the effect over the rail components and the implications on the structure maintenance are presented in Section 2 while Section 3 is dedicated to review the numerical approach, pointing

out its main capabilities and introducing the latest developments with respect to the original constitutive model [1]. Section 4 focuses on the pre-processing operations that precede the simulations, i.e., the materials characterization is described paying special attention to their fatigue response and the built numerical models are presented including a description of the geometry, the finite element mesh used and how the train-induced loads are applied. The results obtained in the simulations are given in Section 5 and similarities are established between them and literature records. Finally, conclusions are drawn for the conducted research and the capabilities and the limitations of the applied methodology are stated in order to provide a full review and set the framework where reliable results can be obtained.

2. Problem statement

Fatigue problems associated to railway infrastructure have been numerous through the years and these actually control to a certain degree the maintenance operations at the rail level like grinding or ballast cleaning and replacement due to the unacceptable material degradation caused during the normal infrastructure operation [18]. This phenomenon is not exclusive of rails and it is convenient to distinguish between the regions where these fatigue problems are detected because, although the origin is similar in all the cases, the corresponding technical and economic consequences are different. Fatigue degradation is detected in vehicle components, mainly wheels but also engines, axles, body shells and suspensions, at subrail elements, including the fastening system, slippers and foundation, at surrounding infrastructure [19] and in rails, mostly on rail heads where contact with wheels takes place. There are many recent publications devoted to the study of these fatigue processes, mainly studying the degradation at the train axles and rails [20, 21, 22, 23, 24, 25, 26, 27, 28], but also on the bogies, the chassis and the engine [29, 30, 31], indicating the relevance of the topic for the railway community. The current research focuses on the HCF degradation processes at rail level, where the proposed constitutive law

has been used to reproduce the fatigue developed at two points of the railway path: a straight section and a crossing of a high-speed track.

2.1. Straight section

Fatigue degradation on these regions can develop at different points of the rail depending on the underlying trigger [18, 32, 33]. Due to the improvements in the steel manufacturing process, the degradation induced by internal inclusion or hydrogen shrinkage defects is not an issue anymore and failure is more related now with fatigue evolution on railheads, i.e. the rolling area. The predominant phenomenon is known as rolling contact fatigue (RCF) [32, 34, 35] which is produced by the normal wheel rolling along the rail. This means that the associated degradation can potentially appear at any point of the rail track although those areas with higher stress concentration, e.g. the inter-space between sleepers, sections in turns or welded sections, are the ones which concentrate the major part of the cases. This results in a superficial deterioration at the railhead level as shown in Figure 1, which can be solved through grinding operations if the problem is rapidly detected, otherwise the rail needs to be replaced.

(a) (b)

Figure 1: Rolling contact fatigue deterioration reported in bibliography: a) RCF microcracks reported by Kalousek [36] and b) fatigue degradation detected in the Medellín subway reported by Alarcón et al. [34].

2.2. Crossing element

Crossings are the elements of the railway system that allow switching the trains from one rail to another when required. These are composed by two parts: the first one controls the transition between tracks through switch units that redirect the train movement and the second part takes charge of accommodating the train on its transition from one rail to the other. Ensuring the smoothness along this transition is not always possible and this can lead to the fatigue degradation of the metal piece that interacts with the train wheel, the so called frog nose. The deterioration here is similar to the one observed on the straight elements, i.e., a spalled region is formed along the frog nose being more important on those points where the first contact with the wheel takes place. Figure 2 shows the degradation experienced by a frog nose placed in the Puertollano high-speed railtrack in Spain.

(a) (b)

Figure 2: Fatigue degradation detected at the frog nose element placed at the Puertollano line. a) General and b) detail views. Source: CIMNE.

The study undergone for the straight section and the crossing element in this paper focuses on the behaviour of the rail and the frog nose, respectively, while trains go through. Therefore, the corresponding numerical simulations intend to reproduce the superficial degradation patterns observed along the rail and exemplified on Figures 1 and 2. The spalling observed on the studied elements appears on these simulations as a progressive loss of the material strength and stiffness at those regions where fatigue degradation is predicted, driving the

material to a fully fatigued-damaged state with fully dissipated fracture energy. The studied scenarios have been selected for their simplicity compared with other areas of the railtrack where fatigue could appear as a second order effect. Therefore, the study here can be focused on the fatigue phenomenon without major interactions of other wearing processes. Finally, although at this stage some simplifications have been taken into account, e.g., nor thermal effects, nor plasticity, nor residual stresses, etc. have been taken into account, the present research can be considered as a starting point in the direction of building a tool for the advanced study of fatigue processes at rail level and it can be useful in the planning of the maintenance campaigns.

3. HCF constitutive law

The HCF constitutive law presented [1] is an extension of the isotropic damage model proposed by Oliver et al. [37]. The underlying model predicts the progressive degradation of the material strength and stiffness once a certain stress threshold is reached.

The isotropic damage model is based on the definition of the damage scalar variable d, which accounts for the stiffness degradation in the material with absence of plastic strains. Therefore, the constitutive response of a material is

$$\boldsymbol{\sigma} = m^0 \frac{\partial \Psi}{\partial \boldsymbol{\varepsilon}} = (1-d)\,\mathbb{C}_0 : \boldsymbol{\varepsilon} = \underbrace{\mathbb{C}_0 : \boldsymbol{\varepsilon}}_{\text{predictive stress, } \sigma_0} - \underbrace{d \cdot \mathbb{C}_0 : \boldsymbol{\varepsilon}}_{\text{damage correction}} \tag{1}$$

where $\boldsymbol{\sigma}$ and $\boldsymbol{\varepsilon}$ are the stress and strain tensors, respectively, $\mathbb{C}_0$ is the undamaged constitutive tensor, m^0 is the material density and Ψ is the free Helmholtz energy which can be formulated in the reference configuration as a function of strains and the damage internal variable [38].

$$\Psi\left(\boldsymbol{\varepsilon}, d\right) = (1-d)\,\frac{1}{2m^0}\left(\boldsymbol{\varepsilon} : \mathbb{C}_0 : \boldsymbol{\varepsilon}\right) \tag{2}$$

This is a direct constitutive model where d is explicitly defined for each stress level and no iterative process is required during the calculation at the integration point level. The damage variable takes values $[0-1]$ from intact to fully

damaged, remaining constant, $\dot{d} = 0$, while the yielding criterion is satisfied, i.e.,

$$\mathbb{F}(\boldsymbol{\sigma}_0) = f(\boldsymbol{\sigma}_0) - \mathcal{K} \leq 0 \tag{3}$$

where $f(\boldsymbol{\sigma}_0)$ is the equivalent predictive stress and $\mathcal{K}$ the material threshold function which is a historical variable of the maximum stress level reached on the material. The equivalent stress is a uniaxial measure of the tensorial stress state which depends on the yield surface chosen. For the purpose of this work, the Von Mises yield surface has been adopted for the steel elements and equivalent stresses are computed as

$$f(\boldsymbol{\sigma}_0) = \sqrt{3J_2} \tag{4}$$

where J_2 is the second invariant of the stress deviator tensor [38, 39]. Therefore, the equivalent predictive stress is computed at each integration point of the structure from the predictive stress $\boldsymbol{\sigma}_0$ and governs the response of the material along the simulation.

When Eq. (3) is not satisfied, the evolution of the damage internal variable is controlled through an exponential softening function [37, 40]

$$d = 1 - \frac{f^0(\boldsymbol{\sigma}_0)}{f(\boldsymbol{\sigma}_0)} \cdot \exp\left[A \cdot \left(1 - \frac{f(\boldsymbol{\sigma}_0)}{f^0(\boldsymbol{\sigma}_0)}\right)\right] \tag{5}$$

where $f^0(\boldsymbol{\sigma}_0) = \mathcal{K}^0$ is the initial equivalent stress threshold and A,

$$A = \left(\frac{g_f \cdot E}{\left(f^0(\boldsymbol{\sigma}_0)\right)^2} - \frac{1}{2}\right)^{-1} \geq 0 \tag{6}$$

is a parameter that guarantees that the available energy for the non-linear process at each Gauss point is equal to the given volumetric fracture energy of the material, $g_f = \frac{G_f}{l_c} = \int_{t=0}^{\infty} \Psi_0 \, \dot{d} \, dt$, where E is the Young's modulus, G_f is the fracture energy, l_c is the characteristic length of the finite element and $\Psi_0 = \dfrac{f^0(\boldsymbol{\sigma}_0)}{2E}$ is the free energy. Figure 3 schematically reflects the main features of this constitutive law in a uniaxial stress-strain chart.

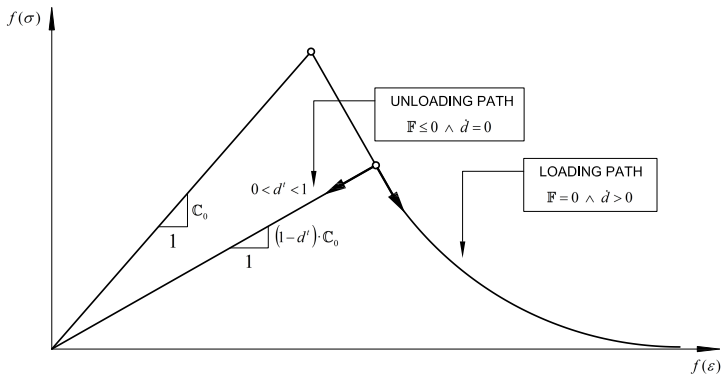

Figure 3: Uniaxial strain-stress scheme of the isotropic damage model.

The absence of plastic strains in HCF processes [1, 15] is the key point in deciding to use the isotropic damage model as the underlying model in the proposed HCF constitutive law. The main modification introduced by this routine affects the isotropic damage yielding criterion definition (Eq. (3)), which is now

$$\mathbb{F}\left(\boldsymbol{\sigma}_0\right) = \frac{f\left(\boldsymbol{\sigma}_0\right)}{f_{red}\left(N_c, R, S_{max},\right)} - \mathcal{K} \leq 0 \tag{7}$$

where f_{red} is the so called *fatigue reduction factor* and ranges from 1 to 0. This parameter takes into account the effect of the acting cyclic load and, consequently, amplifies the stress state depending on the number of cycles applied, N_c, the reversion factor, $R = \dfrac{S_{min}}{S_{max}}$, and the maximum stress generated by the applied load, S_{max}. The number of cycles, N_c, along the simulation is updated based on the evolution of the equivalent stresses at the integration point level, i.e., when maximum and minimum values of the stress are detected this indicates that a new cycle has overcome. Therefore, S_{max}, S_{min} and R variables are updated at each new cycle, if necessary.

Figure 4 compares the performance of the HCF constitutive law assuming that a value of $f_{red} = 0.8$ has been reached in the material with the isotropic damage prediction.

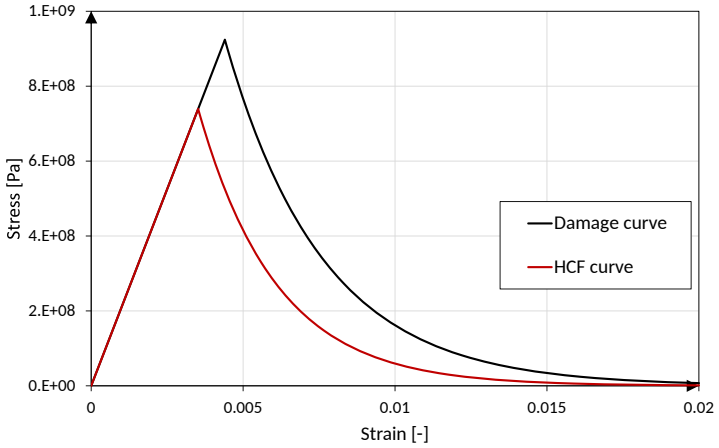

Figure 4: Behaviour at a Gauss Point level with mechanical properties $f^0(\boldsymbol{\sigma}_0) = 924MPa$, $E = 210GPa$ and $g_f = 5MJ/m^3$ and fatigue reduction factor, $f_{red} = 0.8$.

This example helps to understand the immediate effects of the HCF model over the material behaviour. On one hand, the damage threshold diminishes to a new value $\mathcal{K}^* = \mathcal{K} \cdot f_{red}$ ensuring that non-linear processes start below the original yield threshold and, on the other hand, the fracture energy is dissipated not only through the damage process but also through the fatigue mechanism. This is captured in Figure 4 as a variation of the enclosed areas at the stress-strain curves, w_{max}, i.e.,

$$\begin{aligned} &\text{Damage:} \quad w_{max} = g_f \\ &\text{HCF:} \quad\quad w_{max} = g_f \cdot f_{red}^2 \end{aligned} \tag{8}$$

A complete study with the mathematical derivation of the fracture energy dissipated in the HCF process is included in Appendix A.

The definition of the f_{red} factor in the model is done in such a way that it captures the information provided by the widely used S-N curves [41], i.e. predicts the progressive degradation of the material while a cyclic load is applied, resulting in the material failure. In general, this failure condition is materialized accompanied by a rapid evolution of the damage internal variable, d. Mathematically, this is achieved in this work through an exponential function of the

form

$$f_{red}\left(N_c, R, S_{max}\right) = \exp\left\{-B_0\left(R, S_{max}\right) \cdot \left(\log_{10} N_c\right)^{\beta_f^2}\right\} \tag{9}$$

being

$$B_0\left(R, S_{max}\right) = \frac{\ln\left(S_{max}/S_u\right)}{\left(\log_{10} N_f\right)^{\beta_f^2}} \tag{10}$$

a coefficient of the model, N_f the number of cycles to reach failure conditions, S_u the ultimate strength of the virgin material and β_f a material property to be set according to the S-N curves. Therefore, when a cyclic load induces stresses greater than the fatigue limit and below the yield stress, the proposed approach predicts nonlinearities at the corresponding integration points coming from two sources: a first one that induces gradual strength and fracture energy reduction due to the evolution of f_{red} variable and a second one, triggered by the first one, once $N_c = N_f$, where damage propagates and the stiffness reduces. In general, the first non-linear process concentrates the major part of the cycles of the material life while the second non-linear process is rapid and failure takes place soon due to the brittleness of the material at that point. Both of them constitute the whole HCF life and the propagation of this process throughout the numerical model characterizes the degradation mechanism that control the global failure of the studied element.

As stated before, the definition of the f_{red} variable has been done according to the S-N curves which can be fitted in a surface of the type [1]

$$S\left(R, N_c\right) = S_{th}\left(R\right) + \left(S_u - S_{th}\left(R\right)\right) \cdot \exp\left(-\alpha_t\left(R\right) \cdot \left(\log_{10} N_c\right)^{\beta_f}\right) \tag{11}$$

where $S_{th}\left(R\right)$ is the fatigue limit function

$$S_{th}\left(R\right): \begin{cases} |R| \leq 1 \Rightarrow S_{th}\left(R\right) = S_{th}\left(R=-1\right) + \left(S_u - S_e\right) \cdot \left(\dfrac{1+R}{2}\right)^{S_{th,R1}} \\ |R| > 1 \Rightarrow S_{th}\left(R\right) = S_{th}\left(R=-1\right) + \left(S_u - S_e\right) \cdot \left(\dfrac{1+R}{2R}\right)^{S_{th,R2}} \end{cases} \tag{12}$$

that establishes the minimum stress value below which the cyclic load being applied does not induce any fatigue effect in the material, i.e., $\dot{f}_{red} = 0$, $\alpha_t\left(R\right)$

is a parameter that depends on the cyclic load being applied

$$\alpha_t(R): \begin{cases} |R| \leq 1 \Rightarrow \alpha_t(R) = \alpha_f + \left(\dfrac{1+R}{2}\right) \cdot \text{AUX R1} \\ |R| > 1 \Rightarrow \alpha_t(R) = \alpha_f - \left(\dfrac{1+R}{2R}\right) \cdot \text{AUX R2} \end{cases} \tag{13}$$

and $S_{th,R1}$, $S_{th,R2}$, α_f, AUX R1 and AUX R2 are material properties to be calibrated according to the S-N curves.

Through this description of the S-N space, an expression for the N_f function can be obtained, imposing that for any load the f_{red} function and the normalized expression of the S-N curves, $S(R, N_c)/S_u$ are equal, i.e.,

$$\left.\begin{aligned} & f_{red}(N_f, R, S_{max}) = \exp\left\{-\frac{\ln(1/R)\cdot(\log_{10} N_f)^{\beta_f^2}}{(\log_{10} N_f)^{\beta_f^2}}\right\} \\ & \frac{S(R,N_f)}{S_u} = \frac{S_{th}(R)}{S_u} + \left(1 - \frac{S_{th}(R)}{S_u}\right)\cdot\exp\left(-\alpha_t(R)\cdot(\log_{10} N_f)^{\beta_f}\right) \end{aligned}\right\} \Rightarrow$$
$$\Rightarrow N_f(R, S_{max}) = 10^{-\frac{1}{\beta_f\cdot\alpha_t(R)}\cdot\ln\left(\frac{S_{max}-S_{th}(R)}{S_u - S_{th}(R)}\right)} \tag{14}$$

Therefore, the derived fatigue formulation predicts the material behaviour while the cyclic load is applied and its use requires the calibration of 4 to 6 parameters, i.e., α_f, β_f, $S_{th,R1}$ and/or $S_{th,R2}$ and AUX R1 and/or AUX R2. Mathematical meaning can be given to these parameters through Eqs. 9 to 13; α_f and β_f fully characterize the S-N curve for $R = -1.0$ while $S_{th,Ri}$ and AUX Ri with $i = 1,\ 2$ define the S-N surface in the remaining R domain. In particular, $S_{th,Ri}$ defines the fatigue limit function, i.e., the slice of the S-N surface for high N_c values.

An approach based on the native fitting functions available in Matlab [42] is used for the calibration of these parameters. These functions are fed with experimental S-N data to fit the mathematical description of the Wöhler surface stated in Eq. 11. The accuracy of this fitting process depends on the amount of available experimental results, being important to have data for different R and S_{max} values, covering the whole surface domain. In addition to that, as the underlying constitutive law is dedicated to HCF analysis, experimental data obtained for that regime should be weighted to ensure a better fitting

there. Finally, in those scenarios where the amount of experimental data is not sufficient for a good calibration in all the domain, e.g., only values for one particular R are available, the calibrated parameters can still be used to simulate fatigue processes on the surrounding regions of these *well-fitted* areas. The results of the calibration process done for the materials of interest are shown in Section 4.

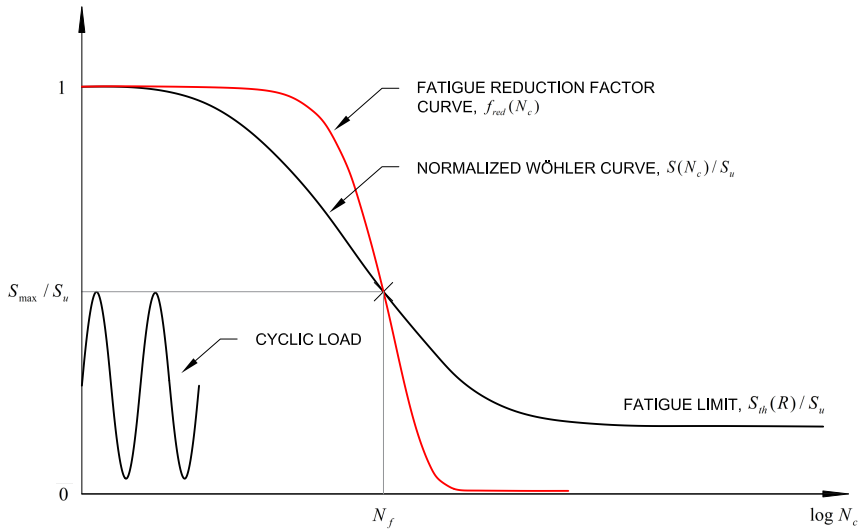

Figure 5: Normalized Wöhler curve and f_{red} evolution for a generic material and a generic load being applied.

Figure 5 helps to understand the relation between the f_{red} and the normalized Wöhler curve functions showing their evolution with respect to the number of cycles, N_c. The normalized S-N curve is generic for the reversion factor, R, of the cyclic load being applied but the f_{red} curve plotted is only valid for the S_{max} level considered. From this sketch, the following relations are deduced

$$\begin{aligned} N_c < N_f \Rightarrow f_{red}\left(N_c, R, S_{max}\right) > S\left(R, N_c\right)/S_u \qquad & \textit{Fatigue regime} \\ N_c \geq N_f \Rightarrow f_{red}\left(N_c, R, S_{max}\right) \leq S\left(R, N_c\right)/S_u \qquad & \textit{Fatigue+damage regime} \end{aligned} \tag{15}$$

which can be extrapolated to the whole reversion factor space.

Finally, this constitutive model takes advantage of the information used to

characterize the fatigue behaviour of metals, i.e., the S-N curves, and predicts the material behaviour during its life before and after reaching N_f, accommodating if necessary any change in the load that is being applied.

The use of this approach is destined to HCF cases where no plastic deformations are expected but where a high amount of cycles are required before reaching failure conditions ($10^5 - 10^7$ cycles). This induces high computational costs and prevents the use of this model even for small cases. In order to overcome this issue, the constitutive law works together with an advance in time (AIT) strategy that allows to quickly skip load cycles before and after damage initiation (see Algorithm 1). By using this strategy, the computational costs significantly reduce and the calculation attention is redirected to the non-linear process. The strategy has been updated since its presentation in Barbu et al. [15] by including new stabilization and jump criteria that control the AIT calculation and by adapting it to allow multi-loaded cases where various cyclic loads are applied, defining independent cycle and period counters per integration point. In addition to this, the efficiency has been improved by parallelizing not only the AIT strategy but the whole HCF constitutive law using the OpenMP application.

Algorithm 1: Advance In Time (AIT) strategy - basic layout

// Calculation at Gauss Point level, i.

$\eta_{1,i} = \left| \dfrac{R^{i+1} - R^i}{R^{i+1}} \right|$ // Reversion factor stabilization norm

$\eta_{2,i} = \left| \dfrac{S^{i+1}_{max} - S^i_{max}}{S^{i+1}_{max}} \right|$ // Maximum stress stabilization norm

if $(d_i > 0)$ **then**

  damage $= true$ // Non-linear process has started at any GP

end

$NF_i = N_{f,i} - N_{c,i}$ // Cycles to failure

// Loop for the elements.

if $(\sum_i \eta_{1,i} < tol. \ \wedge \ \sum_i \eta_{2,i} < tol.)$ **then**

  // Stable conditions reached (AIT strategy ON).

  if $damage == false$ **then**

    $AIT = \min\{NF_i\} \cdot period$ // Skipping the linear phase

  else

    $AIT \sim f(\Delta d^*)$ // Δd^* is a user defined variable that controls the advance in time once damage has initiated at any GP (see Appendix B).

  end

else

  // Unstable conditions (AIT strategy OFF)

  $AIT = 0$

end

$time = time + AIT$ // Updating simulation time

This constitutive law is used in this paper to characterize the behaviour of two types of steels: the pearlitic Grade 900A steel and the Hadfield steel. Pearlitic steels are used in the railway industry due to their high strength, high wear resistance and low cost [43, 44, 45]. In particular, 900A steel is characterized by a high fatigue resistance with a high fatigue limit but a poor fatigue crack growth resistance [43]. This material is used in the construction

of UIC 60 profiles which are used in those tracks with speed limits $> 160 km/h$, including high-speed rail systems [46]. On the other hand, Hadfield steels are alloys with a high content of manganese. This component provides them with high impact strength [47, 48] and thus these steels have been traditionally used in railway crossings.

4. Computational model and materials characterization

The analysis of the two regions described in Section 2 has been done through the Finite Element Method (FEM). Two models have been created in order to study the HCF effects that the continuous traffic circulation has over the rails. The geometries and the finite element meshes have been created using the pre and post-processor tool GiD [49] and the calculations have been performed using the open-source code Kratos Multi-physics [50] where the HCF algorithm presented in Section 3 has been implemented.

4.1. Straight section

The straight section study has been undergone building the $3.1 m$ long railway straight section shown in Figure 6. The model includes the main elements of a standard high-speed railway track, i.e., the rail, the elastomeric pads, the ties, the ballast and the main sub-structure ground layers. The rail profile corresponds to a UIC 60 defined in the EN 13674-1:2002 [51] and a detailed view of the modelled rail is shown in Figure 7.

The model has been constrained according to the confining conditions of the surrounding soil, i.e., limiting the displacements on the bottom of the subsoil material and on the four sides of the ballast and ground layers, and the same hypothesis has been considered to the rail, where the longitudinal displacement has been blocked on both ends. These boundary conditions are sufficient for the undergone analysis considering the localized effect that the applied loads introduce in the model and because of the assumed simplifications (see Section 2).

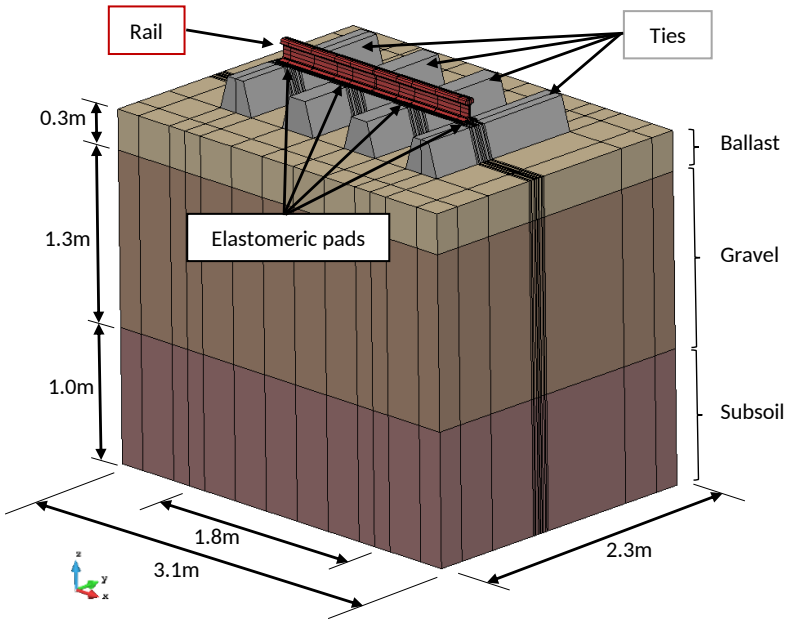

Figure 6: Numerical model of the straight railway section. Main elements and dimensions.

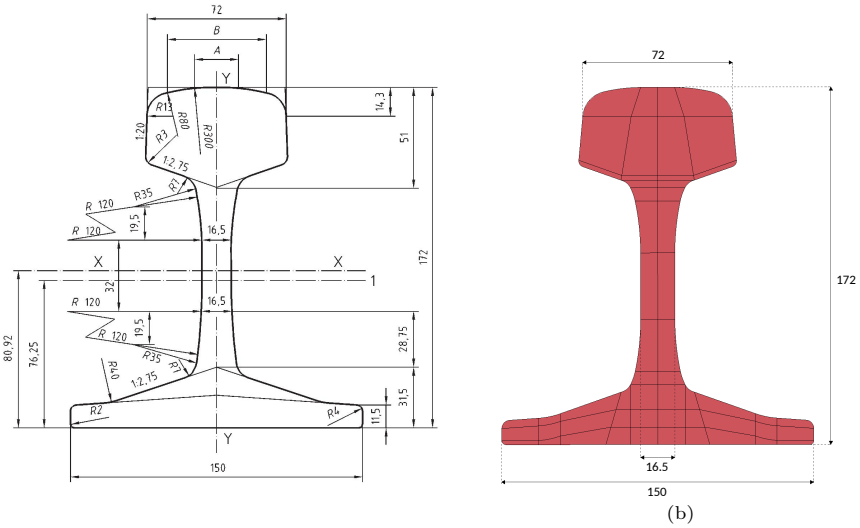

(a) (b)

Figure 7: UIC 60 profile view, a) EN standard scheme [51] and b) model detail. Units in $[mm]$.

The mechanical properties used in the simulation to characterize the behaviour of the straight section model are included in Table 1. These basic properties characterize the elastic response of the structure. This has been considered sufficient for all the elements of the structure except for the rail, where considerably higher stresses are concentrated.

Table 1: Mechanical properties of the materials included in the straight section model.

Element	**Density** $[kg/m^3]$	**Young modulus** [MPa]	**Poisson**
Rail UIC60	7850	210000	0.32
Elastomeric pad	1200	100	0.45
Concrete tie	2200	25000	0.32
Ballast	1390	300	0.27
Gravel	1390	280	0.27
Subsoil	1390	2750	0.27

Therefore, these properties have been complemented with the fatigue characterization done for the pearlitic Grade 900A steel used in the rail. This calibration of the non-linear response has been done by adjusting the control variables of the model to experimental results, as explained in Section 3. For this material, the $R = 0.1$ tensile fatigue tests undergone by Christodoulou et al. [43] have been used. The samples tested there were obtained from rail heads in unused conditions and thus the properties exhibited by the material are suitable for the study of the rail fatigue behaviour. Despite this, the effect that the maintenance operations introduce in the rail along its life [52, 53] are not reflected in these original properties and have not been considered in the undergone study.

Results of the calibration process are summarized in Table 2 and Figure 8 where the values of the HCF constitutive law control variables and the S-N curves for the reversion factor spectra $R \in [0 - 1]$ are shown. Considering that the fitting has been done using only values corresponding to $R = 0.1$, the use of this calibrated material should be limited to fatigue cases where the reversion factor of the applied cyclic loads is close to the experimental one. This condition is satisfied in the undergone analysis as the oscillating load applied in

the straight section model has $R = 0.0$.

Table 2: Pearlitic Grade 900A steel fatigue characterization. HCF model variables for the spectra $R \in [-1; 1]$.

Variable	Value
Su	924 MPa
$S_{th}(R = -1)$	369.1 MPa
α_f	0.0068
β_f	3.20
$S_{th,R1}$	2.00
$AUX\,R1$	0.01

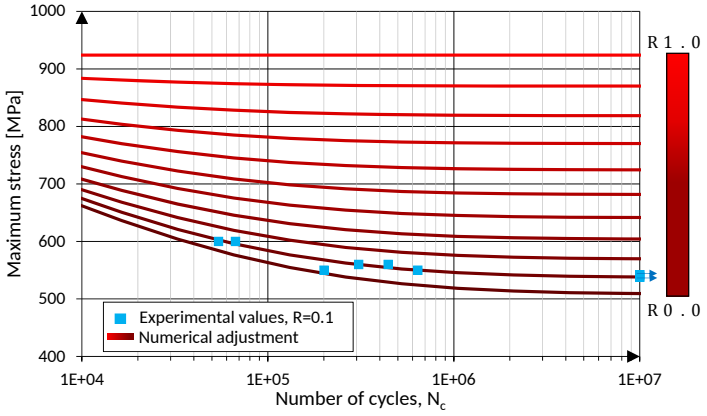

Figure 8: Fatigue calibration of the pearlitic Grade 900A steel according to the experimental results obtained by Christodoulou et al. [43] for $R = 0.1$. Run-outs points are highlighted with arrows.

The mechanical rolling over effect of the train is considered by imposing a cyclic vertical displacement at the mid-span of the space between ties where maximum stresses are generated. This displacement has been introduced through the model of a train wheel as shown in Figure 9 in order to guarantee the correct force distribution over the rail during the simulation. Other actions like thermal or chemical effects are out of the scope of this research and only a displacement which generates a stress state compatible with fatigue is being considered.

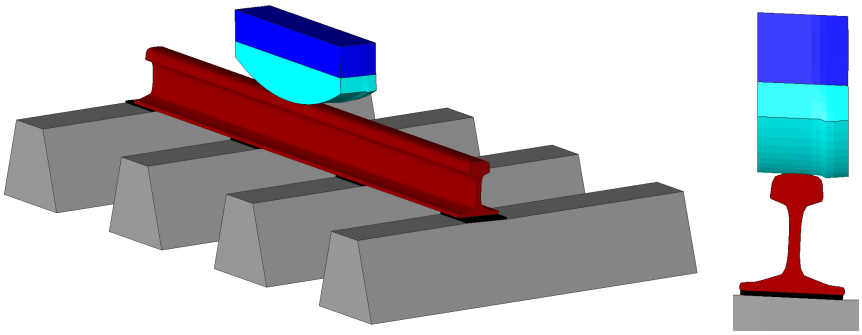

Figure 9: Load application at the straight section model: a) general view and b) section view.

Finally, the finite element mesh of the model has been built using 8-nodded hexahedral elements. Higher mesh density has been provided to the rail element, particularly to the region between ties where the imposed displacement is applied as this is the region where fatigue deterioration is expected. Figure 10 shows this refinement, where $71,400$ elements of the total of $142,309$ hexahedra are concentrated.

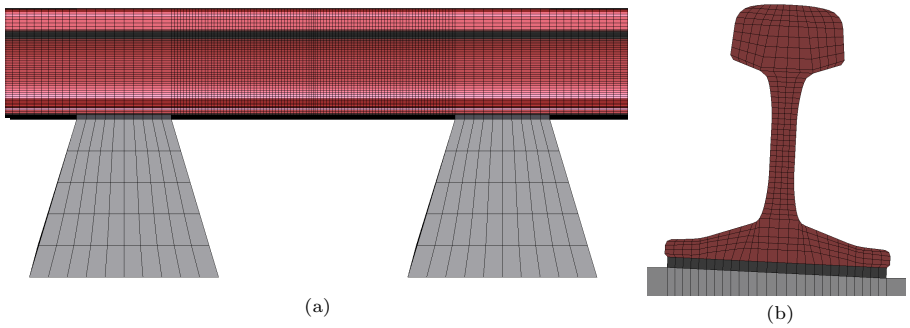

Figure 10: Finite element mesh detail of the rail element, a) elevation view of the refined region between ties where the displacement is imposed and b) section view.

4.2. Crossing element

The crossing element study has been undergone building a $2.1m$ x $2.0m$ model which focuses on the frog nose where fatigue degradation is studied. The model includes the main elements of the crossing system, i.e., elastomeric pads, concrete ties and a $0.3m$ ballast layer as shown in Figure 11. No sub-ballast

soil layers have been considered for this simulation due to the high localization of the phenomenon as will be seen on the results section. The dimensions of all the elements have been adjusted to the Puertollano line crossing element shown in Figure 2.

The corresponding constrictions have been set according to the confining conditions as in the straight section model however, only the downstream end of the frog nose has its longitudinal displacement blocked, while the tip is free. These boundary conditions are again sufficient for the crossing element model due to the localization of the applied loads and because of the assumed simplifications (see Section 2).

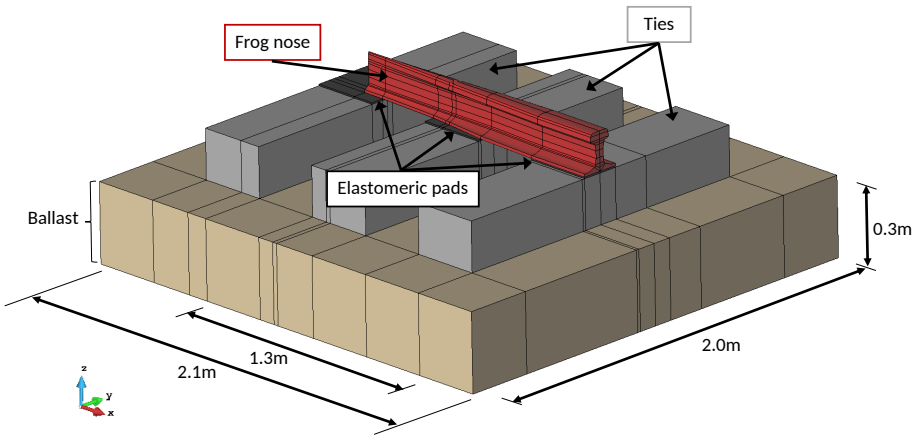

Figure 11: Crossing element numerical model. Main parts and dimensions

The same basic mechanical properties used for the straight section model and shown in Table 1 are used to characterize the materials of the crossing element model and a new calibration of the HCF constitutive law has been done for the manganese steel present in the frog nose. The $R = 0.1$ bending fatigue results obtained by Kang et al. [48] have been used to do this fatigue characterization, where the differences between tension and bending fatigue [54, 55] have been taken into account by defining a $R = 0.1$ S-N curve which predicts earlier failure than the ones obtained through the bending experiments. Results of this calibration process are summarized in Table 3 and Figure 12 where the

values of the HCF constitutive law control variables and the S-N curves for the reversion factor spectra $R \in [0-1]$ are shown. As for the straight section case, the use of this calibrated material should be limited to fatigue cases where the
345 applied cyclic loads have reversion factors close to the experimental one, i.e., $R = 0.1$. This condition is satisfied in the undergone analysis as the oscillating load considered in the frog nose model has $R = 0.0$.

Table 3: Hadfield steel fatigue characterization. HCF model variables for the spectra $R \in [-1; 1]$.

Variable	**Value**
Density	7850 kg/m^3
Young modulus	210000 MPa
Poisson	0.30
Su	1100 MPa
$S_{th}(R=-1)$	300 MPa
α_f	0.0008
β_f	4.46
$S_{th,R1}$	1.58
$AUX\,R1$	-0.00032

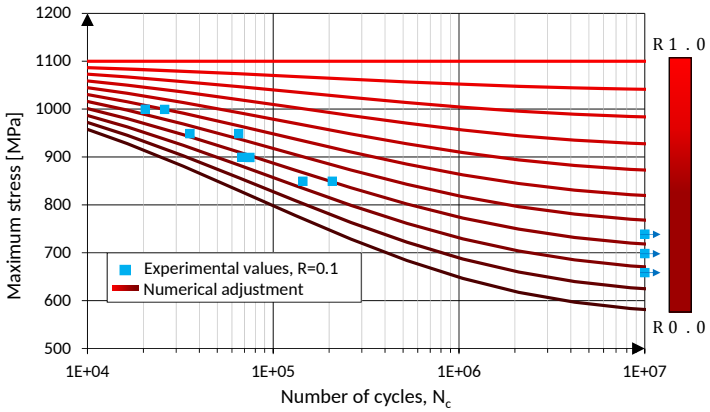

Figure 12: Fatigue calibration of the Hadfield steel used for the frog nose according to the experimental results obtained by Kang et al. [48] for $R = 0.1$. Run-outs points are highlighted with arrows.

The interaction between the wheel and the frog nose has proven to take

place at a distance of $0.47m$ from the tip and it is at this point where the cyclic action has been applied. The application of this external displacement has been performed analogously to the straight section, as shown in Figure 13, and neither thermal nor chemical effects have been considered in this case.

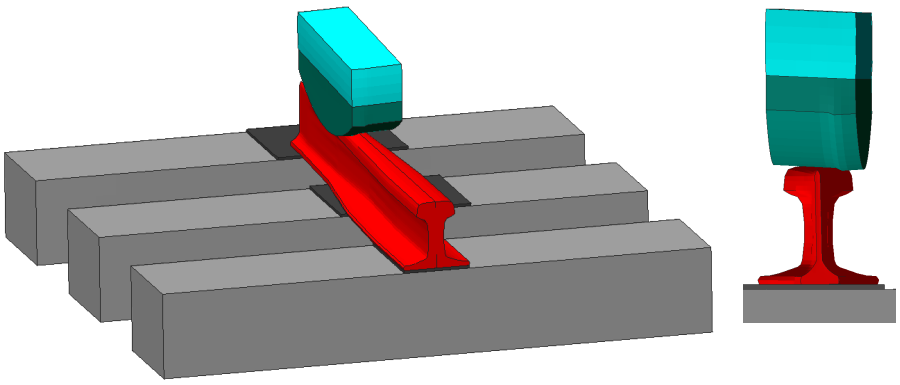

(a) (b)

Figure 13: Load application at the crossing element model: a) general view and b) section view.

Finally, the finite element mesh of the model has been build using 8-nodded hexahedral elements. Higher mesh density has been provided to the frog nose element where fatigue study is intended, particularly to the section located at $0.47m$ from the tip where the wheel-rail interaction takes place. Figure 10 shows this refined region, where $47,648$ elements of the total of $82,686$ hexahedra are concentrated.

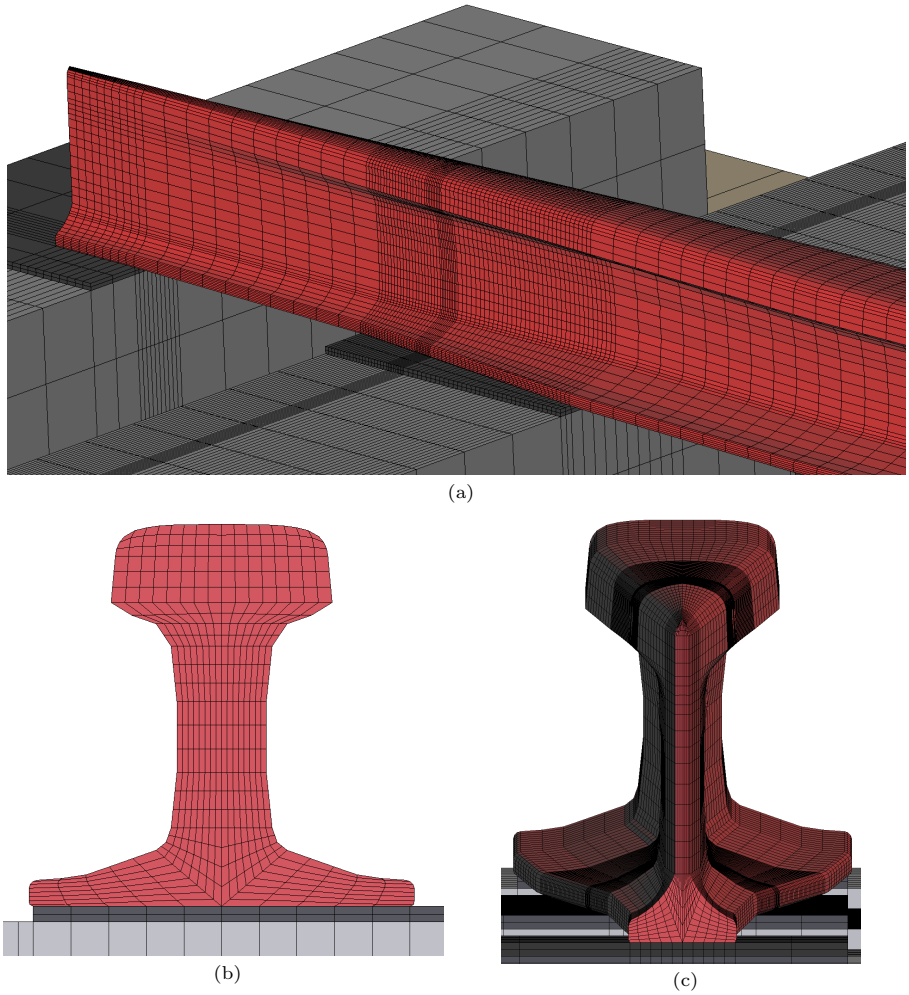

Figure 14: Finite element mesh detail of the frog nose, a) general of the frog nose refined region where the displacement is imposed, b) section view and c) frontal view of the frog nose finite element mesh.

5. Results

In this section the results obtained for the previous scenarios are presented. A preliminary control case has been included where one of the tensile experiments used on the fatigue characterization of the pearlitic steel is reproduced. The main features of the HCF constitutive law are reviewed through this ini-

tial case where result are already known. Figure 15 shows the model built and an overall view of the finite element mesh used. Displacements in one end of the sample have been blocked while on the opposite end a cyclic displacement has been imposed to reproduce the experiment conditions of a normalized axial fatigue test according to ASTM E466 [56].

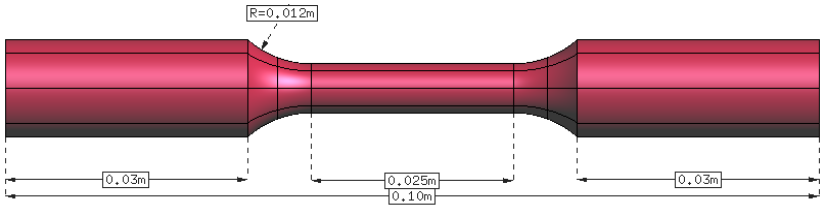

(a)

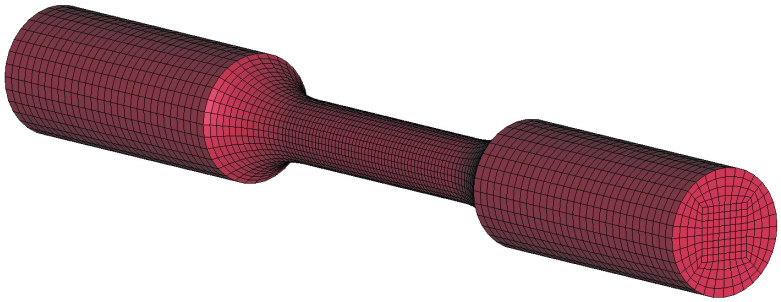

(b)

Figure 15: Model of the samples used in the tensile fatigue experiments undergone by Christodoulou et al. [43]: a) geometry with main dimensions and b) finite element mesh made of 29,051 8-nodded hexahedra.

On this simulation stresses oscillate between $55.9 - 559$MPa. For this stress rate, damage initiates after $318,663$ cycles and rapidly evolves and propagates. Damage is triggered by the decrease of the f_{red} variable on those areas where stress exceeds the fatigue limit. This *susceptible to fatigue* region extends throughout the entire narrowed section as shown in Figure 16, however, two rings showing higher degradation level are recognizable and set the starting point for damage propagation.

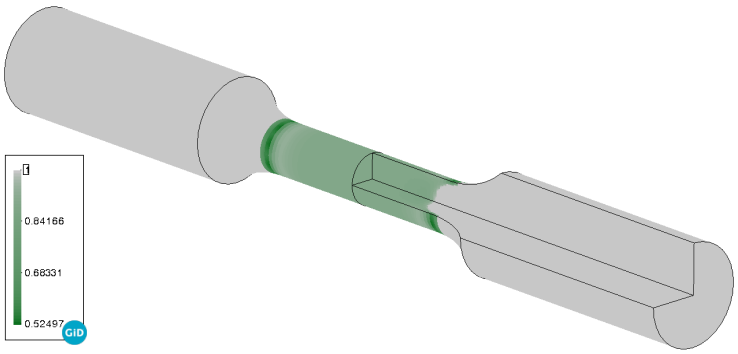

Figure 16: Fatigue reduction factor distribution on the sample when damage is about to start, $N_C = 318,663$.

The fracture energy exhaustion caused by the fatigue process generates a fragile fracture, which induces a rapid evolution and propagation of the damage internal variable, as shown in Figure 17. Damage propagates symmetrically on the sample, starting superficially but evolving to the centre and finally creating a full damaged plane across the sample after $1,026$ cycles. Note that these $318 - 319k$ cycles to failure are on the same range that the ones obtained experimentally and shown in Figure 8 when a $R = 0.1$ cyclic load with maximum stress $\simeq 560$MPa is applied.

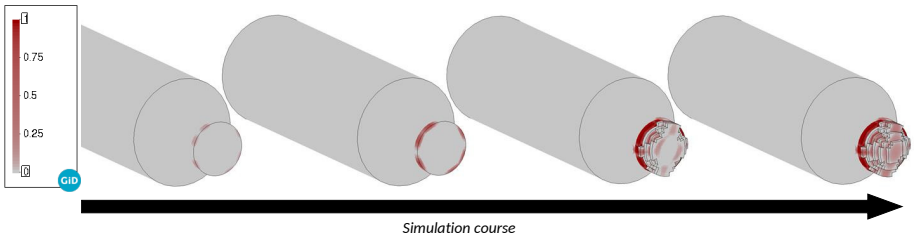

Figure 17: Damage internal variable, d, evolution along the simulation, from $N_C = 318,663$ to $319,689$.

Now the results for the straight section and the crossing element are presented. The introduced action is an oscillating vertical displacement ($R = 0.0$) at the rail and the frog nose heads, as stated previously. The way that this external action has been introduced reproduces the physics of the problem but

the magnitude imposed has been defined pursuing the main objective of the paper, i.e., ensuring the fatigue degradation of the structure and studying it through the HCF constitutive law presented.

Firstly, the resultant tensile stress distribution obtained by the applied load is presented for both scenarios. These stresses are the ones that induce fatigue on the structure if they surpass the corresponding fatigue limit, S_{th}, and are pointed out in Figure 18. Some of these areas match with the affected regions gathered in literature [33, 34], e.g., the surroundings of the region in contact with the train wheel, the bottom of the rail head or the union between the web and the foot. This fact points out the suitability of the built cases to study the phenomenon of interest.

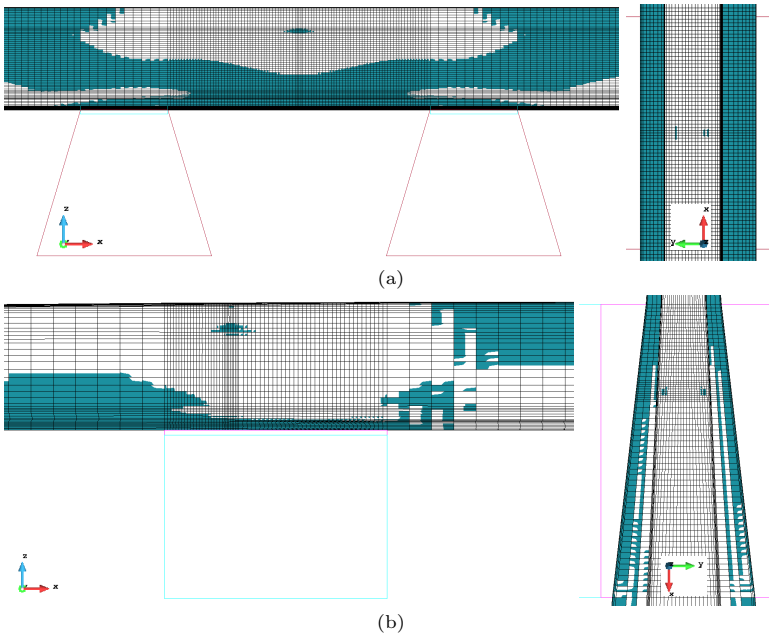

Figure 18: Rail regions working under tension in a) the straight section model and b) the crossing element model.

Maximum stresses are observed on the rail head surface of both models, which will lead to superficial damage as the one shown in Figures 1 and 2. The equivalent stress distribution in this area is complex; it is characterized by

a noticeable compressed bulb as consequence of the external load that rapidly dissipates and in the vicinity of this area, small tensed regions appear induced by the shear components of the stress. This behaviour can be observed in Figure 19 where equivalent stresses are plotted for the instant when displacement is maximum in absolute value. The maximum tensile stress obtained in each case surpasses the corresponding fatigue limit, i.e., $S_{th}(R = 0) = 508.20$MPa in the pearlitic steel and $S_{th}(R = 0) = 568.51$MPa in the manganese steel, but this is exclusive of these superior regions where fatigue degradation will concentrate. Despite this, this can change once damage starts and redistribution on the stress field takes place, potentially creating new fatigued areas.

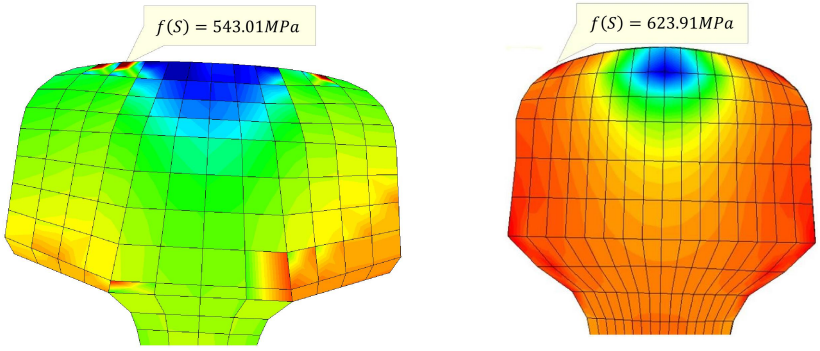

(a) (b)

Figure 19: Equivalent stress distribution on for the instant when maximum load is being applied a) on the rail head of the straight section model and b) on the frog nose head.

Figure 20 shows the damage distribution on the straight section and the crossing element models after $264,408$ and $2,562,626$ cycles, respectively. Beyond this point the degradation stabilizes for the current cases. Despite the simplifications considered for these simulations, the type of degradation observed can explain some of the deterioration patterns registered in literature, reflecting the potential of the applied formulation for the study of the HCF phenomenon.

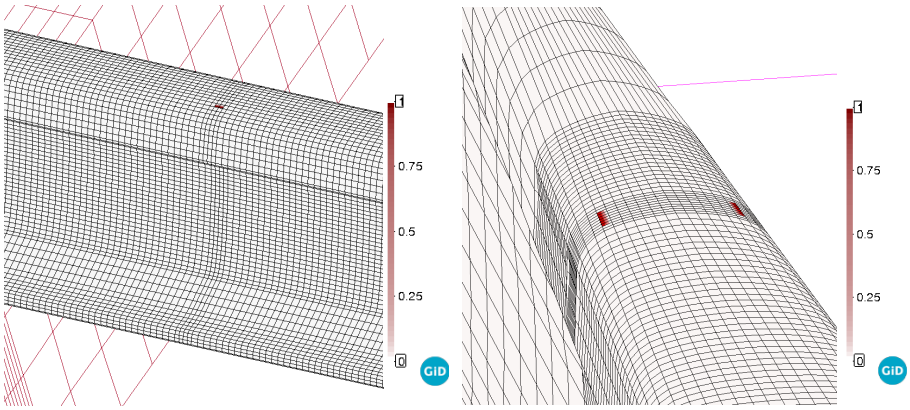

(a) (b)

Figure 20: Damage internal variable distribution by the end of the simulation on a) the straight section model and b) the crossing element model.

Finally, the behaviour of the model can be checked by plotting the evolution of the problem variables along the simulations as shown in Figure 21. These charts are built using the information from the most stressed integration point in each model. The stress curve intersects the S-N curve at a point quite close to the corresponding fatigue limits, which explains the small degradation observed in Figure 20. Obtaining a generalized fatigued area through the simulation would be possible when higher loads take place or by considering the passing-through effect of the train along the rail. Despite this, damage initiation and its rapid evolution due to the fracture energy dissipation motivated by the cyclic load, can be observed in both scenarios once the S-N curve is reached, i.e., after the corresponding N_f cycles computed as a function of the maximum stress, S_{max} and the reversion factor, R, as stated in Section 3. The swap between the normal advancing mode and the AIT strategy is also noticeable in both cases, allowing to take the problem right to the beginning of the damage non-linearities after only 3 cycles. This reflects the amount of computational-time saved by the use of this technology.

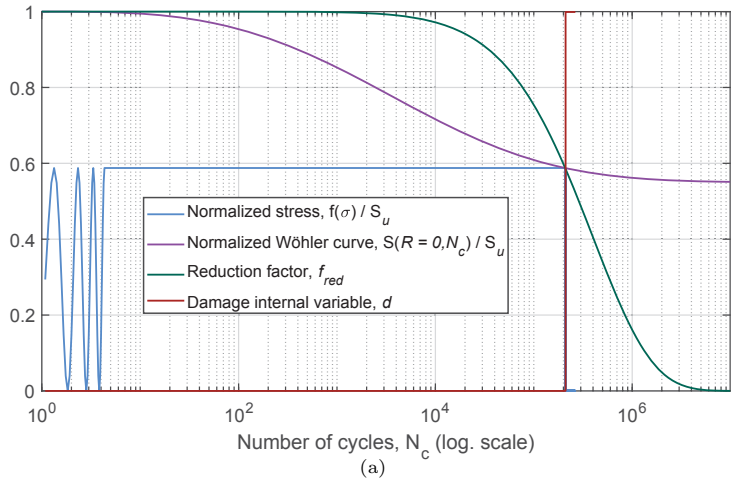

(a)

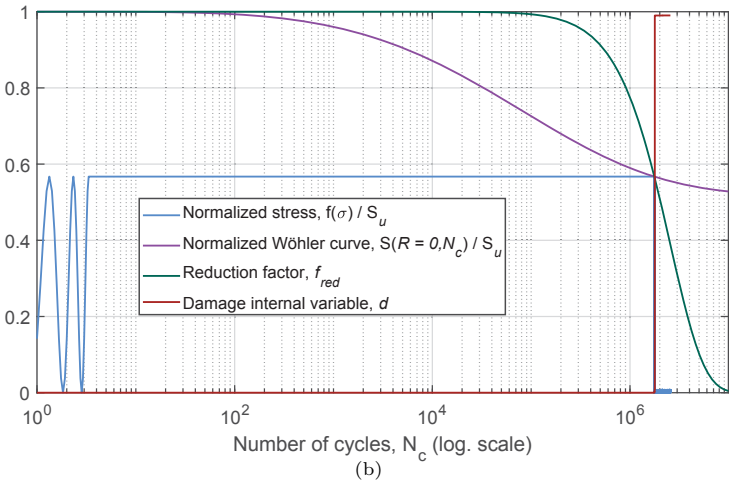

(b)

Figure 21: Evolution of the internal variables of the problem on a) the straight section model and b) the crossing element model.

6. Conclusions

In this research, an isotropic damage based HCF constitutive law has been presented and its performance has been shown through several examples. Although the approach was introduced on previous publications, latest improvements as well as newly relevant demonstrations for the constitutive law are presented. Among others, the code parallelization, the enhancement of the *AIT* strategy and the quantification of the dissipated fracture energy along with the

fatigue process are introduced in the document. In addition to that, the application of the methodology into the railway field has been studied for the first time and the arisen strengths and weakness can be pointed out.

Even though several simplifications have been considered for the studied problems, interesting results have been obtained which highlight the main features of the applied methodology. A complete study of the fatigue phenomenon historically observed on railway industry should include among others: plastic behaviour of materials, residual stresses at rails, thermal actions, stochastic imperfections distribution on materials that are responsible of some specific failures, time effects like delayed settlements induced by ballast degradation, effect of the aluminothermic welds on rails, etc. which were out of the scope of the undergone research. On one hand, some of these can be indirectly addressed through the used approach but a wider material characterization would be then required. This is the case of these phenomena that induce a preexisting quantifiable degradation in the material and reduce their fatigue performance, like the presence of residual stresses. On the other hand, the inclusion of other phenomena necessary depends on the extension of the presented approach which constitutes future lines of work. These include: switching from a deterministic to a stochastic approach in the fatigue analysis by affecting the calibration process followed in the HCF characterization, or extending the methodology to address coupled thermo-mechanical problems which will increase the added value of the presented methodology on the study of fatigue phenomenon for railway elements.

Despite this, at this moment the model is appropriate for the study of a large number of scenarios governed by the HCF phenomenon, allowing to efficiently predict the initiation and propagation of the damage on the model while loads are applied, independently of their typology, i.e., uniform or cyclic and the uniformity, i.e., $R \neq const.$ Using the presented approach, the rail regions reported in literature as susceptible to fatigue degradation have been identified, the degradation observed at the rail head and the frog nose has been simulated and the differed material degradation and the brittle fracture that characterize

the physics of the problem have been captured.

7. Acknowledgments

This work has been done within the framework of the RESILTRACK (IDI-20171003) project: *resilencia de infraestructuras ferroviarias frente a cambio climático*. This project has received funding from the Spanish Government. The work has been also supported by the Spanish Government program $FPU17/04196$. The authors gratefully acknowledge all the received support.

Appendix A. Fracture energy dissipation in the HCF process

Here it is derived the expression for the variation of the available fracture energy when the HCF constitutive law is used. The expression for the total dissipated energy in the isotropic damage constitutive law [38] is

$$w_t^{max} = \int_{t=0}^{\infty} \Xi \, dt = \int_{t=0}^{\infty} \Psi_0 \dot{d} \, dt = \int_{\bar{\sigma}^0}^{\bar{\sigma}^{max}} \underbrace{\frac{[\bar{\sigma}]^2}{2 \cdot E}}_{\text{free energy}} \frac{\partial \hat{G}\left(\bar{\sigma}\right)}{\partial \bar{\sigma}} \, d\bar{\sigma} = g_f \tag{A.1}$$

where $\bar{\sigma} \equiv f\left(\boldsymbol{\sigma}_0\right)$ is the predictive equivalent stress, $\bar{\sigma}^0 \equiv f^0\left(\boldsymbol{\sigma}_0\right)$ is the yield stress, $\bar{\sigma}^{max} \equiv f^{max}\left(\boldsymbol{\sigma}_0\right)$ is the predictive stress level when the fracture energy has been fully dissipated, E is the Young modulus and $\hat{G} \equiv d$ is the damage internal variable function. The result, $w_t^{max} = g_f$ is independent of the definition chosen for $\hat{G}$. Two cases are studied here: the linear and the exponential descriptions of the damage.

$$\begin{aligned} &\underline{\text{Linear case}}: && d = \left(1 - \frac{\bar{\sigma}^0}{\bar{\sigma}}\right) \cdot \frac{1}{1 - A} && \wedge && A = \frac{\left(\bar{\sigma}^0\right)^2}{2 g_f E} \\ &\underline{\text{Exponential case}}: && d = 1 - \frac{\bar{\sigma}^0}{\bar{\sigma}} \cdot \exp\left[A \cdot \left(1 - \frac{\bar{\sigma}}{\bar{\sigma}^0}\right)\right] && \wedge && A = \frac{1}{\dfrac{g_f E}{\left(\bar{\sigma}^0\right)^2} - \dfrac{1}{2}} \end{aligned} \tag{A.2}$$

The $\bar{\sigma}^{max}$ value reached in each scenario is $\bar{\sigma}_{lin.}^{max} = \dfrac{\bar{\sigma}^0}{A}$ for the linear description and $\bar{\sigma}_{exp.}^{max} = +\infty$ for the exponential case. These stress values are obtained from Eq. A.2 when $d = 1.0$.

The extrapolation to the HCF case is done by affecting Eqs. A.1 and A.2 with f_{red}. This function results in a *reduction* of the normal yield surface of the underlying damage model as a consequence of the fatigue process. Finally,

Linear:

$$\begin{aligned} w_t^{max,\,HCF} &= \int_{t=0}^{\infty} \Xi\, dt = \int_{t=0}^{\infty} \Psi_0 \dot{d}\, dt = \int_{\bar{\sigma}^0 \cdot f_{red}}^{\bar{\sigma}^0 \cdot f_{red}/A} \frac{[\bar{\sigma}]^2}{2E} \frac{\partial \hat{G}\,(\bar{\sigma})}{\partial \bar{\sigma}}\, d\bar{\sigma} = \\ &= \int_{\bar{\sigma}^0 \cdot f_{red}}^{\bar{\sigma}^0 \cdot f_{red}/A} \frac{[\bar{\sigma}]^2}{2E} \frac{\bar{\sigma}^0 \cdot f_{red}}{[\bar{\sigma}]^2\,(1-A)}\, d\bar{\sigma} = \left. \frac{\bar{\sigma} \cdot \bar{\sigma}^0 \cdot f_{red}}{2E \cdot (1-A)} \right|_{\bar{\sigma}^0 \cdot f_{red}}^{\bar{\sigma}^0 \cdot f_{red}/A} = \\ &= \frac{\left[\bar{\sigma}^0\right]^2 \cdot f_{red}^2}{2EA} = g_f \cdot f_{red}^2 \end{aligned} \tag{A.3}$$

Exponential:

$$\begin{aligned} w_t^{max,\,HCF} &= \int_{t=0}^{\infty} \Xi\, dt = \int_{t=0}^{\infty} \Psi_0 \dot{d}\, dt = \int_{\bar{\sigma}^0 \cdot f_{red}}^{+\infty} \frac{[\bar{\sigma}]^2}{2E} \frac{\partial \hat{G}\,(\bar{\sigma})}{\partial \bar{\sigma}}\, d\bar{\sigma} = \\ &= \int_{\bar{\sigma}^0 \cdot f_{red}}^{+\infty} \frac{[\bar{\sigma}]^2}{2E} \left(\frac{A}{\bar{\sigma}} + \frac{f_{red}\,\bar{\sigma}^0}{[\bar{\sigma}]^2} \cdot \exp\left[A \cdot \left(1 - \frac{\bar{\sigma}}{f_{red}\,\bar{\sigma}^0} \right) \right] \right) d\bar{\sigma} = \\ &= -\left. \frac{f_{red}\,\bar{\sigma}^0 \left(2 \cdot f_{red}\,\bar{\sigma}^0 + A\,\bar{\sigma} \right) \cdot \exp\left[\frac{A \cdot (1-\bar{\sigma})}{f_{red}\,\bar{\sigma}^0} \right]}{2AE} \right|_{\bar{\sigma}^0 \cdot f_{red}}^{+\infty} = \\ &= \frac{f_{red}^2 \left[\bar{\sigma}^0\right]^2 (A+2)}{2AE} = g_f \cdot f_{red}^2 \end{aligned} \tag{A.4}$$

Appendix B. Computing the advance in time (AIT) once damage has initiated

In order to smartly advance once the internal damage variable has initiated, i.e., N_f has been reached at some GP, the user defines the Δd^*-parameter which controls the AIT. The time increment that analytically induces a variation of the damage internal variable $\Delta d = \Delta d^*$ is computed through this input. The relation between the time increment and the variation of the damage internal variable is obtained using d and f_{red} definitions (Eq. (5), (9)) and that the stress state in the HCF regime is $\dfrac{f\,(\boldsymbol{\sigma}_0)}{f_{red}}$.

The damage:

Linear case

$$d = \left(1 - \frac{f_{yield}}{f(\sigma)}\right) \cdot \frac{1}{1-A} \Rightarrow \quad f_{red} = \left[1 - d \cdot (1+A)\right] \frac{f(\boldsymbol{\sigma}_0)}{f^0(\boldsymbol{\sigma}_0)} \tag{B.1}$$

Exponential case

$$\begin{aligned}
& d = 1 - \frac{f^0(\boldsymbol{\sigma}_0) \cdot f_{red}}{f(\boldsymbol{\sigma}_0)} \cdot \exp\left[A \cdot \left(1 - \frac{f(\boldsymbol{\sigma}_0)}{f^0(\boldsymbol{\sigma}_0) \cdot f_{red}}\right)\right] \\
\Rightarrow & \frac{(1-d) \cdot f(\boldsymbol{\sigma}_0)}{f^0(\boldsymbol{\sigma}_0) \cdot f_{red}} = \exp\left[A \cdot \left(1 - \frac{f(\boldsymbol{\sigma}_0)}{f^0(\boldsymbol{\sigma}_0) \cdot f_{red}}\right)\right] \\
\Rightarrow & \ln\left(\frac{(1-d) \cdot f(\boldsymbol{\sigma}_0)}{f^0(\boldsymbol{\sigma}_0)}\right) + \ln\left(\frac{1}{f_{red}}\right) = A \cdot \left(1 - \frac{f(\boldsymbol{\sigma}_0)}{f^0(\boldsymbol{\sigma}_0) \cdot f_{red}}\right) \\
\Rightarrow & \frac{A \cdot f(\boldsymbol{\sigma}_0)}{f^0(\boldsymbol{\sigma}_0) \cdot f_{red}} + \ln\left(\frac{1}{f_{red}}\right) = A - \ln\left(\frac{(1-d) \cdot f(\boldsymbol{\sigma}_0)}{f^0(\boldsymbol{\sigma}_0)}\right) \\
\Rightarrow & \exp\left[\frac{A \cdot f(\boldsymbol{\sigma}_0)}{f^0(\boldsymbol{\sigma}_0) \cdot f_{red}}\right] \cdot \frac{1}{f_{red}} = \frac{\exp(A) \cdot f^0(\boldsymbol{\sigma}_0)}{(1-d) \cdot f(\boldsymbol{\sigma}_0)} \\
\Rightarrow & f_{red} = \frac{A \cdot f(\boldsymbol{\sigma}_0)}{f^0(\boldsymbol{\sigma}_0)} \cdot \frac{1}{\omega\left(\frac{A \cdot \exp(A)}{1-d}\right)}
\end{aligned} \tag{B.2}$$

Where $\omega(\cdot) = \sum_{n=1}^{\infty} \frac{(-n)^{n-1}}{n!} (\cdot)^n$ is the Lambert function. And the fatigue reduction factor:

$$f_{red} = \exp\left\{-B_0 \cdot (\log_{10} N_c)^{\beta_f^2}\right\} \Rightarrow \quad N_c = 10^{\left[-\frac{\ln(f_{red})}{B_0}\right]^{1/\beta_f^2}} \tag{B.3}$$

Therefore,

$$\begin{aligned}
\text{Linear case:} \quad \Delta N_c &= 10^{\left[-\frac{\ln\left(\frac{[1-\Delta d^* \cdot (1+A)] \cdot f(\boldsymbol{\sigma}_0)}{f^0(\boldsymbol{\sigma}_0)}\right)}{B_0}\right]^{1/\beta_f^2}} \\
\text{Exponential case:} \quad \Delta N_c &= 10^{\left[-\frac{\ln\left(\frac{A \cdot f(\boldsymbol{\sigma}_0)}{f^0(\boldsymbol{\sigma}_0)} \cdot \frac{1}{\omega\left(\frac{A \cdot \exp(A)}{1-\Delta d^*}\right)}\right)}{B_0}\right]^{1/\beta_f^2}}
\end{aligned} \tag{B.4}$$

References

[1] S. Oller, O. Salomón, and E. Oñate. A continuum mechanics model for mechanical fatigue analysis. *Computational Materials Science*, 32(2):175–195, 2005. ISSN 0927-0256. doi: https://DOI.org/10.1016/j.commatsci.2004.08.001.

[2] H. Zenner and K. Hinkelmann. August Wöhler – founder of fatigue strength research. *Steel Construction*, 12(2):156–162, 2019. doi: https://DOI.org/10.1002/stco.201900011.

[3] ASTM E1823-13. Standard terminology relating to fatigue and fracture testing. Technical report, ASTM International, West Conshohocken, PA, 2013. URL `www.astm.org`.

[4] L.G Barbu. *Numerical simulation of fatigue processes. Application to steel and composite structures*. PhD thesis, Universitat Politècnica de Catalunya (UPC), Spain, 2015. URL `http://hdl.handle.net/10803/386479`.

[5] R.I. Stephens, A. Fatemi, R. Stephens, and H.O. Fuchs. *Metal Fatigue in Engineering*. 01 2000.

[6] Y. Bai and W.L. Jin. Part 3: Fatigue and fracture. In *Marine Structural Design (Second Edition)*, pages 477–578. Butterworth-Heinemann, Oxford, second edition edition, 2016. ISBN 978-0-08-099997-5. doi: https://DOI.org/10.1016/B978-0-08-099997-5.00025-3.

[7] L.G. Barbu, X. Martinez, S. Oller, and A.H. Barbat. Validation on large scale tests of a new hardening–softening law for the barcelona plastic damage model. *International Journal of Fatigue*, 81:213–226, 2015. ISSN 0142-1123. doi: https://DOI.org/10.1016/j.ijfatigue.2015.07.031.

[8] L.G. Barbu, S. Oller, X. Martinez, and A.H. Barbat. High-cycle fatigue constitutive model and a load-advance strategy for the analysis of unidirectional fiber reinforced composites subjected to longitudinal loads.

Composite Structures, 220:622–641, 2019. ISSN 0263-8223. doi: https://DOI.org/10.1016/j.compstruct.2019.04.015.

[9] H. E. Boyer. *Atlas of Fatigue Curves*. ASM International, 1986. ISBN 978-0-87170-214-2.

[10] J.G. Kaufman. Properties of aluminum alloys: Tensile, creep, and fatigue data at high and low temperatures. 1 1999. URL `https://www.osti.gov/biblio/6305846`.

[11] X. Martinez, S. Oller, L.G. Barbu, A.H. Barbat, and A.M.P. de Jesus. Analysis of ultra low cycle fatigue problems with the barcelona plastic damage model and a new isotropic hardening law. *International Journal of Fatigue*, 73:132–142, 2015. ISSN 0142-1123. doi: https://DOI.org/10.1016/j.ijfatigue.2014.11.013.

[12] C. Nagel, A. Sondag, and M. Brede. 4 - Designing adhesively bonded joints for wind turbines. In *Adhesives in Marine Engineering*, Woodhead Publishing Series in Welding and Other Joining Technologies, pages 46–71. Woodhead Publishing, 2012. ISBN 978-1-84569-452-4. doi: https://DOI.org/10.1533/9780857096159.1.46.

[13] L. Susmel. High-cycle fatigue of notched plain concrete. *Procedia Structural Integrity*, 1:2–9, 2016. ISSN 2452-3216. doi: https://DOI.org/10.1016/j.prostr.2016.02.002.

[14] R. Talreja and C.V. Singh. *Damage and Failure of Composite Materials*. Cambridge University Press, 2012. ISBN 9781139016063. doi: https://DOI.org/10.1017/CBO9781139016063.

[15] L.G. Barbu, S. Oller, X. Martinez, and A. Barbat. High cycle fatigue simulation: A new stepwise load-advancing strategy. *Engineering Structures*, 97:118–129, 2015. ISSN 0141-0296. doi: https://DOI.org/10.1016/j.engstruct.2015.04.012.

[16] R. Alessi, S. Vidoli, and L. De Lorenzis. A phenomenological approach to fatigue with a variational phase-field model: The one-dimensional case. *Engineering Fracture Mechanics*, 190:53–73, 2018. ISSN 0013-7944. doi: https://DOI.org/10.1016/j.engfracmech.2017.11.036.

[17] P. Carrara, M. Ambati, R. Alessi, and L. De Lorenzis. A framework to model the fatigue behavior of brittle materials based on a variational phase-field approach. *Computer Methods in Applied Mechanics and Engineering*, 361:112731, 2020. ISSN 0045-7825. doi: https://DOI.org/10.1016/j.cma.2019.112731.

[18] L. Lesley. 2 - Fatigue in railway and tramway track. In *Fatigue in Railway Infrastructure*, pages 20–57. Woodhead Publishing, 2009. ISBN 978-1-85573-740-2. doi: https://DOI.org/10.1533/9781845697020.20.

[19] P.M.R. Lewis and K. Reynolds. Forensic engineering: a reappraisal of the Tay Bridge disaster. *Interdisciplinary Science Reviews*, 27(4):287–298, 2002. doi: 10.1179/030801802225005725.

[20] Y. Hu, S. Wu, P.J. Withers, H. Cao, P. Chen, Y. Zhang, Z. Shen, T. Vojtek, and P. Hutař. Corrosion fatigue lifetime assessment of high-speed railway axle ea4t steel with artificial scratch. *Engineering Fracture Mechanics*, 245:107588, 2021. ISSN 0013-7944. doi: https://doi.org/10.1016/j.engfracmech.2021.107588.

[21] T. Vojtek, P. Pokorný, I. Kuběna, L. Náhlík, R. Fajkoš, and P. Hutař. Quantitative dependence of oxide-induced crack closure on air humidity for railway axle steel. *International Journal of Fatigue*, 123:213–224, 2019. ISSN 0142-1123. doi: https://doi.org/10.1016/j.ijfatigue.2019.02.019.

[22] S.C. Wu, Z.W. Xu, G.Z. Kang, and W.F. He. Probabilistic fatigue assessment for high-speed railway axles due to foreign object damages. *International Journal of Fatigue*, 117:90–100, 2018. ISSN 0142-1123. doi: https://doi.org/10.1016/j.ijfatigue.2018.08.011.

[23] D. Regazzi, S. Beretta, and M. Carboni. An investigation about the influence of deep rolling on fatigue crack growth in railway axles made of a medium strength steel. *Engineering Fracture Mechanics*, 131:587–601, 2014. ISSN 0013-7944. doi: https://doi.org/10.1016/j.engfracmech.2014.09.016.

[24] H.M. El-sayed, M. Lotfy, H.N. El-din Zohny, and H.S. Riad. Prediction of fatigue crack initiation life in railheads using finite element analysis. *Ain Shams Engineering Journal*, 9(4):2329–2342, 2018. ISSN 2090-4479. doi: https://doi.org/10.1016/j.asej.2017.06.003.

[25] R.M. Nejad, K. Farhangdoost, and M. Shariati. Three-dimensional simulation of rolling contact fatigue crack growth in UIC60 rails. *Tribology Transactions*, 59(6):1059–1069, 2016. doi: 10.1080/10402004.2015.1134738.

[26] P. Gurubaran, M. Afendi, M.A. Nur Fareisha, M.S. Abdul Majid, I. Haftirman, and M.T.A. Rahman. Fatigue life investigation of UIC 54 rail profile for high speed rail. 908:012026, oct 2017. doi: 10.1088/1742-6596/908/1/012026.

[27] Z. Popović and V. Radović. Rolling contact fatigue of rails. Belgrade, 04 2016. Conference: The III International Scientific and Professional Conference. "CORRIDOR 10 – A sustainable way of integrations".

[28] L. Xin, V.L. Markine, and I.Y. Shevtsov. Numerical procedure for fatigue life prediction for railway turnout crossings using explicit finite element approach. *Wear*, 366-367:167–179, 2016. ISSN 0043-1648. doi: https://doi.org/10.1016/j.wear.2016.04.016. Contact Mechanics and Wear of Rail / Wheel Systems, CM2015, August 2015.

[29] J.W. Seo, H.M. Hur, H.K. Jun, S.J. Kwon, and D.H. Lee. Fatigue design evaluation of railway bogie with full-scale fatigue test. *Advances in Materials Science and Engineering*, page 11, 2017. doi: https://doi.org/10.1155/2017/5656497.

[30] A. Ekberg and E. Kabo. Risk of fatigue of train car chassis due to pressure waves between meeting trains. Technical report, Chalmers University of Technology, 2020.

[31] A. Ktari, N. Haddar, and H.F. Ayedi. Fatigue fracture expertise of train engine crankshafts. *Engineering Failure Analysis*, 18(3):1085–1093, 2011. ISSN 1350-6307. doi: https://doi.org/10.1016/j.engfailanal.2011.02.007.

[32] R.A. Smith. 1 - Fatigue and the railways: an overview. In *Fatigue in Railway Infrastructure*, pages 1–19. Woodhead Publishing, 2009. ISBN 978-1-85573-740-2. doi: https://DOI.org/10.1533/9781845697020.1.

[33] S. Tamargo, J.M. Duart, and J.I. Verdeja. El carril. Soldabilidad y fatiga. In *III Congreso de Historia Ferroviaria. Fundación de los Ferrocarriles Españoles*, 2003.

[34] G.I. Alarcón, J. Sanchez, J. Santa, and A. Toro. Identificación de mecanismos de desgaste en rieles de vía comercial del metro de Medellín. *Revista Colombiana de Materiales*, pages 72–77, may 2014. ISSN 2256-1013.

[35] E. Magel. Rolling contact fatigue: a comprehensive review. *NRC Publications Archive. U.S. Department of Transportation. Federal Railroad Administration*, 2011. doi: 10.4224/23000318.

[36] J Kalousek. Keynote address: light to heavy, snail to rocket. *Wear*, 253(1): 1–8, 2002. ISSN 0043-1648. doi: https://DOI.org/10.1016/S0043-1648(02)00076-5.

[37] J. Oliver, M. Cervera, S. Oller, and J. Lubliner. Isotropic damage models and smeared crack analysis of concrete. In *Second International Conference on Computer Aided Analysis and Design of Concrete Structures*, volume 2, pages 945–958, 1990.

[38] S. Oller. Nonlinear dynamics of structures. 01 2014. doi: 10.1007/978-3-319-05194-9.

[39] E.S. Neto, D. Peric, and D.R.J. Owen. *Computational methods for plasticity*. ISBN: 978-0-470-69452-7. Wiley, 2008.

[40] S. Oller, A.H. Barbat, E. Oñate, and A. Hanganu. A damage model for the seismic analysis of building structures. In *Congreso Mundial de Ingeniería Antisísmica, Madrid*, 1992.

[41] C. Li, S. Wu, J. Zhang, L. Xie, and Y. Zhang. Determination of the fatigue P-S-N curves – A critical review and improved backward statistical inference method. *International Journal of Fatigue*, 139, 2020. ISSN 0142-1123. doi: https://DOI.org/10.1016/j.ijfatigue.2020.105789.

[42] MATLAB. *version 9.7.0 (R2019b)*. The MathWorks Inc., Natick, Massachusetts, 2019.

[43] P.I. Christodoulou, A.T. Kermanidis, and G.N. Haidemenopoulos. Fatigue and fracture behavior of pearlitic Grade 900A steel used in railway applications. *Theoretical and Applied Fracture Mechanics*, 83:51–59, 2016. ISSN 0167-8442. doi: https://DOI.org/10.1016/j.tafmec.2015.12.017. ICEAF-IV Engineering Against Failure.

[44] J. M. Duart, J. A. Pero-Sanz, and J. I. Verdeja. Carriles para alta velocidad. comportamiento en fatiga. *Revista de Metalurgia*, 41(1):66–72, 02 2005. doi: 10.3989/revmetalm.2005.v41.i1.188.

[45] S. Maya Johnson, A. Ramirez, and A. Toro. Fatigue crack growth rate of two pearlitic rail steels. *Engineering Fracture Mechanics*, 138, 03 2015. doi: 10.1016/j.engfracmech.2015.03.023.

[46] A. López. *Infraestructuras ferroviarias*. Barcelona : Edicions UPC, 2010, 2010. ISBN 978-84-9880-415-7.

[47] S. Bhattacharyya. A friction and wear study of hadfield manganese steel. *Wear*, 9(6):451–461, 1966. ISSN 0043-1648. doi: https://DOI.org/10.1016/0043-1648(66)90136-0.

[48] J. Kang, F.C. Zhang, X.Y. Long, and B. Lv. Cyclic deformation and fatigue behaviors of Hadfield manganese steel. *Materials Science and Engineering: A*, 591:59–68, 2014. ISSN 0921-5093. doi: https://DOI.org/10.1016/j.msea.2013.10.072.

[49] R. Ribó, M. Pasenau, E. Escolano, J.S. Ronda, and A. Coll. *GiD user manual*. CIMNE, 2007.

[50] P. Dadvand, R. Rossi, and E. Oñate. An object-oriented environment for developing finite element codes for multi-disciplinary applications. *Archives of Computational Methods in Engineering*, 17:253–297, 2010. ISSN 1886-1784. doi: https://DOI.org/10.1007/s11831-010-9045-2.

[51] EN 13674-1:2002. Railway applications - Track - Rail - Part 1: Vignole railway rails 46kg/m and above. Standard, European Committee for Standardization, Brussels, November 2002.

[52] C. Zhao, J. Li, W. Fan, Y. Liu, and W. Wang. Experimental and simulation research on residual stress for abrasive belt rail grinding. *The International Journal of Advanced Manufacturing Technology*, 109:129–142, 2020. ISSN 1433-3015. doi: 10.1007/s00170-020-05664-5.

[53] L.M. Huang, H.H. Ding, S.Y. Zhang, K. Zhou, J. Guo, Q.Y. Liu, and W.J. Wang. Simulation research on temperature field and stress field during rail grinding. *Proceedings of the Institution of Mechanical Engineers, Part F: Journal of Rail and Rapid Transit*, pages 1–13, 2021. doi: 10.1177/0954409720984568.

[54] T. Hassan and Z. Liu. On the difference of fatigue strengths from rotating bending, four-point bending, and cantilever bending tests. *International Journal of Pressure Vessels and Piping*, 78(1):19–30, 2001. ISSN 0308-0161. doi: https://DOI.org/10.1016/S0308-0161(00)00080-6.

[55] S. S. Manson. Fatigue: A complex subject—Some simple approximations.

Experimental Mechanics, 5:193–226, 1965. ISSN 1741-2765. doi: https://DOI.org/10.1007/BF02321056.

[56] ASTM E466-15. Standard practice for conducting force controlled constant amplitude axial fatigue tests of metallic materials. Technical report, ASTM International, West Conshohocken, PA, 2015. URL `www.astm.org`.

View publication stats